Atomically Precise Single Metal Oxide Cluster Catalyst with Oxygen-Controlled Activity

Xinzhe Li, Na Guo, Zhongxin Chen, Xin Zhou, Xiaoxu Zhao, Yonghua Du, Lu Ma, Yiyun Fang, Haomin Xu, Huimin Yang, Wei Yu, Shangchen Lu, Mingjiao Tian, Qian He, Kian Ping Loh, Shibo Xi,* Chun Zhang,* and Jiong Lu*

Single cluster catalysts (SCCs) consisting of atomically precise metal nanoclusters dispersed on supports represent a new frontier of heterogeneous catalysis. However, the ability to synthesize SCCs with high loading and to precisely introduce non-metal atoms to further tune their catalytic activity and reaction scope of SCCs have been longstanding challenges. Here, a new interface confinement strategy is developed for the synthesis of a high density of atomically precise Ru oxide nanoclusters (Ru_3O_2) on reduced graphene oxide (rGO), attributed to the suppression of diffusion-induced metal cluster aggregation. Ru_3O_2/rGO exhibits a significantly enhanced activity for oxidative dehydrogenation of 1,2,3,4-tetrahydroquinoline (THQ) to quinoline with a high yield (≈86%) and selectivity (≈99%), superior to Ru and RuO_2 nanoparticles, and homogeneous single/multiple-site Ru catalysts. In addition, Ru_3O_2/rGO is also capable of efficiently catalyzing more complex oxidative reactions involving three reactants. The theoretical calculations reveal that the presence of two oxygen atoms in the Ru_3O_2 motif not only leads to a weak hydrogen bonding interaction between the THQ reactant and the active site, but also dramatically depletes the density of states near the Fermi level, which is attributed to the increased positive valence state of Ru and the enhanced oxidative activity of the Ru_3O_2 cluster for hydrogen abstraction.

1. Introduction

The emergence of atomically precise single cluster catalysts (SCCs) has triggered a second wave in heterogeneous catalysis since the concept of single-atom catalysts (SACs) was coined in 2010.[1–4] This new class of advanced catalyst materials is expected to bridge the gap between SACs and conventional metal nanoparticle (NP) based catalysts, not only for fundamental research but also for practical applications.[5–8] Intensive global research over the last decade has made tremendous progress in SACs for a wide range of catalytic transformations.[9–11] Although SACs with a single-metal active site allow for maximized atomic utilization efficiency, this also limits the catalytic scope of SACs, which often lack sufficient activity for organic transformations that involve two or multiple reactants.

In contrast to SACs, SCCs consisting of atomically dispersed metal clusters, typically made up of several metal atoms anchored on catalytic supports, not only offer higher tunability in chemical

X. Z. Li, Z. X. Chen, X. X. Zhou, Y. Y. Fang, H. M. Xu, H. M. Yang, W. Yu, K. P. Loh, C. Zhang, J. Lu
Department of Chemistry
National University of Singapore
3 Science Drive 3, Singapore 117543, Singapore
E-mail: phyzc@nus.edu.sg; chmluj@nus.edu.sg
N. Guo,[+] C. Zhang
Department of Physics
National University of Singapore
2 Science Drive 3, Singapore 117542, Singapore
X. Zhao
School of Materials Science and Engineering
Nanyang Technological University
Singapore 639798, Singapore

Y. H. Du, L. Ma
National Synchrotron Light Source II
Brookhaven National Lab
Upton, NY 11973, USA
S. C. Lu, M. J. Tian, Q. He
Department of Materials Science and Engineering
National University of Singapore
Singapore 117574, Singapore
S. B. Xi
Institute of Chemical and Engineering Sciences
Agency for Science
Technology and Research (A*STAR)
1 Pesek Road, Jurong Island, Singapore 627833, Singapore
E-mail: xi_shibo@partner.nus.edu.sg

composition and atomic arrangements of active sites but also provide multiple adsorption sites for tackling complex reaction systems.[2–4,6,8,12,13] A great tunability in atomic structures and electronic properties in SCCs allows for the design of advanced catalyst materials that can simultaneously activate different reactants to accelerate various elementary reaction steps for chemical transformation. Despite rapid progress in this field, the synthesis of SCCs with high loading, as well as the control of precisely doping of metal clusters to further tune the catalytic activity and reaction scope of SCCs have been recognized as major challenges. Common methods reported for the synthesis of SCCs often involve the deposition of molecular precursors with multinuclear metal molecules on various supports via the impregnation method followed by subsequent removal of ligands.[14–18] However, a lower diffusion barrier of metal clusters than that of ligand removal often results in significant aggregation of individual metal clusters during thermal heating. To suppress the diffusion-induced aggregation, the loading of metal cluster precursors has to be limited to an extremely low level. Therefore, the majority of SCCs synthesized so far have limited metal loadings, typically <0.5 wt.%.[14,15,17–20] In addition, the majority of SCCs reported consist of metal clusters anchored on the surface.[15–19,21] The ability to further introduce non-metal species into the anchored cluster can further modify the valence state of the metal cluster and expand their catalytic scope, which however, remains elusive.
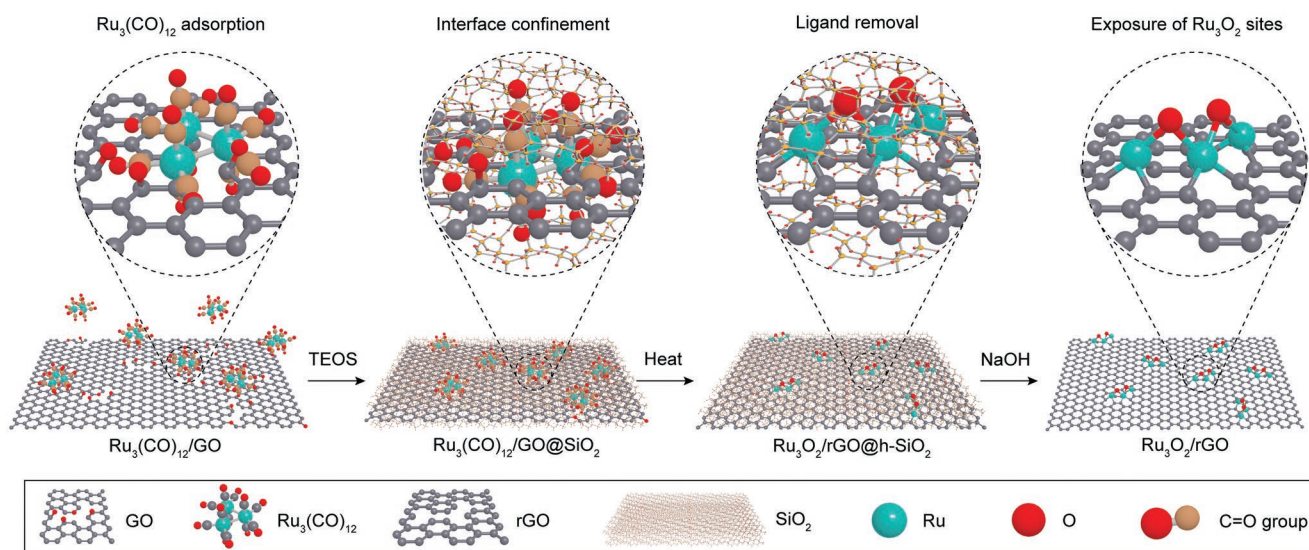
Here, we report an interface confinement strategy to fabricate a high density (≈4.5 wt.%) of atomically precise single metal oxide cluster (Ru_3O_2) anchored onto the reduced graphene oxides (rGO) for efficient oxidative dehydrogenation of 1,2,3,4-tetrahydroquinoline (THQ) to quinoline with a significantly enhanced activity, a high yield (≈86%) and selectivity (≈99%), superior to Ru NPs, RuO_2 NPs, and homogeneous single/multiple-site Ru catalysts. In addition, Ru_3O_2/rGO can efficiently catalyze more complex oxidative reactions involving three reactants, as demonstrated in the synthesis of imines and Cavosonstat derivative (a F508del-CFTR mutation treatment medicine) via Friedländer reaction. Our theoretical

investigation reveals a weak hydrogen bond interaction between THQ and Ru_3O_2 motif facilitates the reactions. This is in sharp contrast to the strong covalent bonding interaction between THQ adsorbed both over the single Ru_1 site and Ru(0001). In addition, two bridging oxygen atoms in Ru_3O_2 dramatically deplete the density of states near Fermi level, which increases the positive valence state of Ru and the oxidative activity of Ru_3O_2 cluster for the hydrogen abstraction process.

2. Results

2.1. Synthesis and Characterization of Ru_3O_2/rGO SCCs with High Loading

Here, we developed a new strategy for the fabrication of high-loading Ru_3O_2 anchored onto defective rGO, which relies on the interface confinement strategy to suppress diffuse-induced metal aggregation. This synthetic route reported here involves the following critical steps (**Figure 1**). First, $Ru_3(CO)_{12}$ molecular precursors containing a Ru_3 trimer center are deposited on the surface of GO to form a $Ru_3(CO)_{12}$/GO composite via impregnation (see Experimental Section). In the second step, $Ru_3(CO)_{12}$/GO was encapsulated by amorphous SiO_2 layers generated in situ via a controlled tetraethyl orthosilicate (TEOS)'s hydrolysis, leading to the formation of a sandwiched structure of $Ru_3(CO)_{12}$/GO@SiO_2. Subsequently, heating sample up to 250 °C triggers the thermal reduction of GO into rGO and ligand removal of $Ru_3(CO)_{12}$ (Figure S1, Supporting Information), whereby Ru_3 cluster can be anchored over defect sites of rGO via bonding with carbon/oxygen atoms (denoted as Ru_3O_2/rGO@h-SiO_2). Finally, the encapsulated SiO_2 film can be removed by soaping in NaOH aqueous solution to expose Ru_3O_2 active sites (the structural identification of active sites of Ru_3O_2/rGO will be discussed in the later section). Interface confinement of metal clusters by encapsulated SiO_2 film is expected to suppress diffusion-induced aggregation of Ru atoms into NPs at an increased metal loading during thermal


Figure 1. Schematic illustration of interface confinement strategy for the fabrication of high-density Ru_3O_2/rGO catalysts.

annealing. As a result, such a strategy allows for the synthesis of Ru_3O_2/rGO with high metal loadings up to ≈4.5 wt.%, beyond which aggregated Ru clusters will be formed on rGO (Figure S2, Supporting Information). In contrast, the maximal loading obtained via conventional method without interface confinement is determined to be ≈0.1 wt.%, beyond that, Ru NPs tend to form as revealed in TEM images (Figure S3, Supporting Information). In addition, defective GO support provides an abundance of anchoring sites with strong interaction with $Ru_3(CO)_{12}$ precursors, which is beneficial to immobilize a high density of Ru_3O_2 sites during the material synthesis (Figure S4, Supporting Information).

To probe their morphology and microstructure, we carried out the electron microscope characterization of as-prepared materials. The heterogeneous nucleation process of TEOS around $Ru_3(CO)_{12}$/GO via a liquid–crystal template mechanism ensures a uniform encapsulation of $Ru_3(CO)_{12}$/GO by SiO_2 layers, which results in the formation of $Ru_3(CO)_{12}$/GO@SiO_2 (Figure S5, Supporting Information).[22,23] Both Ru_3O_2/rGO@h-SiO_2 and Ru_3O_2/rGO retain 2D-like layered morphology

(Figures S6 and S7, Supporting Information). Atomic force microscopy measurement further reveals a thickness of ≈4 nm for representative Ru_3O_2/rGO films (Figure S8, Supporting Information). The absence of Ru NPs in Ru_3O_2/rGO as evidenced in TEM images (Figure S9, Supporting Information) and supported by XRD data (Figure S10, Supporting Information) suggests that the spatial confinement strategy can efficiently prevent the aggregation of Ru clusters into NPs during the heat treatment.

We then performed the state-of-the-art aberration-corrected high-angle annular dark-field scanning TEM (HAADF-STEM) to image atomic arrangements of Ru species in Ru_3O_2/rGO (Figure S11, Supporting Information). Despite the challenges in imaging (beam sensitive) and resolving specific structures of these Ru species due to the overlap effect, our result does reveal the presence of a high density of atomically dispersed Ru atoms without any aggregated clusters or Ru NPs (**Figure 2**a). Moreover, the majority of Ru atoms adopt a trimer configuration (blue circles in Figure 2a) distributed over the entire rGO support. Elemental mapping by energy-dispersive X-ray
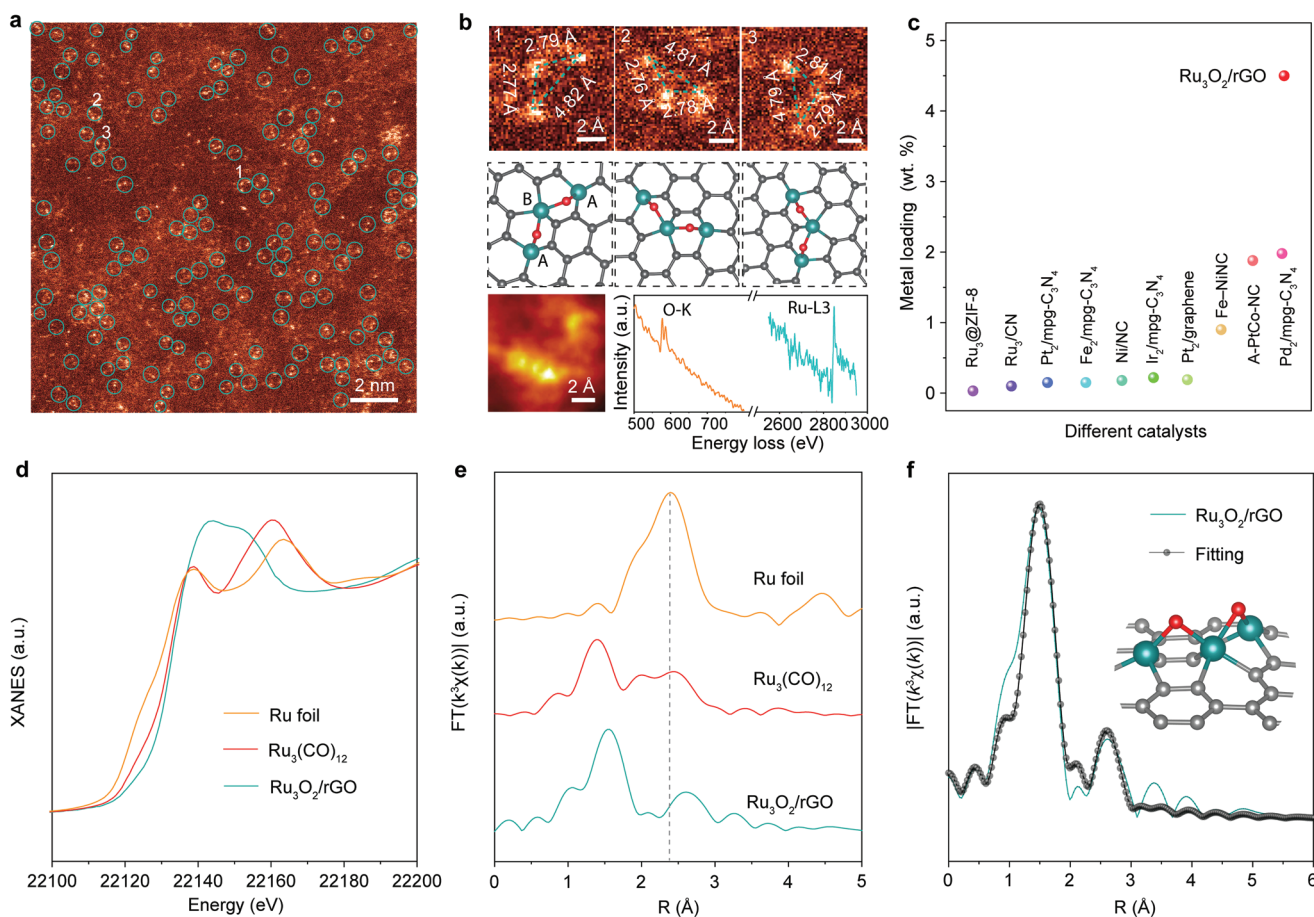
Figure 2. Local structural characterization of Ru_3O_2/rGO catalysts via HAADF-STEM, XANES and EXAFS. a) Aberration-corrected HAADF-STEM image of as-prepared Ru_3O_2/rGO catalysts. b) Top: magnified HAADF-STEM images revealing the atomic structures of three representative Ru_3O_2 labeled as 1, 2, and 3 in (a); Middle: the corresponding structural models of three Ru_3O_2. The symbols A and B in the model refer to the terminal and middle Ru atom, respectively; Bottom: HAADF-STEM image of a Ru_3 trimer and the corresponding EELS of O K-edge and Ru L_3-edge. c) Comparison of metal loading of Ru_3O_2/rGO with other SCCs in previous reports. d) Ru K-edge XANES spectra and e) FT-EXAFS spectrum of Ru foil, $Ru_3(CO)_{12}$, and Ru_3O_2/rGO, respectively. f) EXAFS fitting of Ru_3O_2/rGO at R space. The proposed atomic structure of Ru_3O_2/rGO was inserted in (f), and the black, red, and cyan color represents the C, O, and Ru atoms, respectively.

spectroscopy further confirms a relatively uniform element distribution without forming large aggregates (Figure S12, Supporting Information). Atomic arrangements of three typical Ru trimers (labeled as 1, 2, 3 in Figure 2a) are examined in close detail. The distance of two adjacent Ru atoms is determined to be ≈2.78 Å, while two terminal Ru atoms are separated by a larger distance of ≈4.81 Å (top panel in Figure 2b). A direct imaging of atomic arrangement provides crucial information to validate the proposed atomic structure of Ru_3 center in Ru_3O_2/rGO, which will be discussed in Section 2.2. The theoretical model of Ru_3O_2/rGO displayed in the middle panel of Figure 2b reveals that the distance of two adjacent or terminal Ru atoms matches well with that observed in HAADF-STEM images. The statistical analysis of the nearest-neighbor Ru–Ru distance obtained from >200 Ru_3 sites reveals an averaged value of 0.28 nm (Figure S13, Supporting Information), consistent with the theoretical distance between the middle and terminal Ru atom in the Ru_3O_2/rGO model. It is noted that a small portion of Ru species is imaged as isolated single atoms, presumably resulting from the dissociation of the Ru_3O_2 upon the electron beam radiation during HAADF-STEM measurement or the alignment of Ru clusters with the direction of the electron beam probe.[15,24] To further investigate the local chemical environment of Ru atoms, spatial-dependent electron energy loss spectra (EELS) measurements were conducted over Ru_3 site (bottom panel of Figure 2b), revealing the coexistence of Ru-L_3 edge (2838 eV) and O-K edge (532 eV) related peaks. This further confirms that individual Ru_3O_2 active site indeed contains both Ru and O atoms. It is noted that Ru loading in our Ru_3O_2/rGO catalysts prepared by the interface confinement method can be up to ≈4.5 wt.%, much higher than that of other reported SCCs prepared via different approaches including impregnation and atomic layer deposition (Figure 2c).[14,15,17–20,24–27]

To explore the chemical valence state and local coordination environment of Ru atoms in Ru_3O_2/rGO catalysts, X-ray absorption near-edge structure (XANES) spectroscopy and extended X-ray absorption fine structure (EXAFS) spectroscopy measurements were carried out (Figure 2d,e).[28,29] The normalized Ru K-edge XANES spectra of the Ru_3O_2/rGO catalysts and other reference materials, including $Ru_3(CO)_{12}$, $Ru(acac)_3$, and Ru foil reveal that Ru_3O_2/rGO shows a similar adsorption profile with the commercial $Ru(acac)_3$ (Figure S14, Supporting Information). This suggests a valence state of Ru(III) in Ru_3O_2/rGO. The XPS spectrum (Figure S15, Supporting Information) reveals a binding energy of 382.94 eV for O 1s, indicating the valence state of O(II) in Ru_3O_2/rGO. Fourier-transformed (FT) k^3-weighted EXAFS spectrum of Ru_3O_2/rGO resolves a dominant peak at ≈1.56 Å, attributed to the scattering from the first shell of Ru-C/O, in contrast to the dominant features peaked at ≈1.38 Å and ≈2.39 Å for $Ru_3(CO)_{12}$ and Ru foil, respectively. Notably, the peak related to the direct metallic Ru—Ru bond is not observed in the EXAFS spectrum of Ru_3O_2/rGO. A fitting to the experimental Ru EXAFS data was then performed (Figure 2f and Figure S16 in Supporting Information), which reveals that the average bond length between terminal Ru and C/O atoms is ≈2.01 Å, and the coordination number of terminal Ru is ≈4.1. The distance of the second sphere by the Ru–Ru path is ≈2.81 Å (the corresponding coordination number is ≈2.4), significantly longer than that of direct metallic Ru–Ru bond in

Ru foil (≈2.67 Å). All above results reveal that an additional O atom may bridge the Ru–Ru bond to form a Ru—O—Ru—O—Ru structure (Ru_3O_2 active site) anchored over the rGO support.

We then performed density functional theory (DFT) calculations to further confirm the atomic structure of the active site and its bonding configuration with support. Based on the above analysis of HAADF-STEM, statistics of Ru atom distance distributions, EELS, EXAFS data, and plausible metal atom coordination mechanism, we proposed several possible atomic structures of active sites over defective rGO support for DFT structural relaxation (Figure S17, Supporting Information), and found that Ru_3O_2 containing the Ru—O—Ru—O—Ru structure is a reasonable structure, wherein each Ru atom in Ru_3O_2 bonds to adjacent three carbon atoms in rGO and bridging oxygen atom (inset in Figure 2f). In addition, the separation of two adjacent Ru atoms is determined to be 2.75 Å, in good agreement with the STEM results (Figure 2b). The bond lengths of Ru–O and Ru–C determined in this Ru_3O_2/rGO model are also consistent with the EXAFS fitting results (Table S1, Supporting Information). The structural stability of Ru_3O_2/rGO from a theoretical perspective is also investigated (Figure S18, Supporting Information), indicating the good stability of the Ru_3O_2 cluster on rGO supports.

2.2. Catalytic Activity of Ru_3O_2/rGO

We then evaluated the unique catalytic properties of Ru_3O_2 using a model heterogeneous reaction involving the oxidative dehydrogenation of THQ to quinoline, due to the following reasons: i) quinoline as the final product has been widely used in pharmaceuticals and other bioactive compounds[30]; ii) it involves two reactants (THQ and O_2), making it ideally feasible system to probe their co-adsorption, activation, and subsequent dehydrogenation, whereby the synergistic effect between multiple metal atoms in SCCs can be better reflected; iii) this model reaction can provide mechanistic insights to expand the catalyst scope of Ru_3O_2/rGO for more complex organic reactions such as synthesis of imines and Cavosonstat derivative via Friedländer reaction that involve three reactants. The catalytic performance of high-density Ru_3O_2/rGO for the oxidative dehydrogenation of THQ to quinoline was evaluated in mesitylene solvent under ambient conditions. As shown in **Figure 3**a, Ru_3O_2/rGO catalysts exhibit a high yield (≈86%) and selectivity (≈99%) toward the formation of quinoline after 18 h, outperforming all the reference catalysts under the same reaction conditions, including heterogeneous commercial Ru/C (10 wt.%), RuO_2, homogeneous $Ru_3(CO)_{12}$ and $Ru(acac)_3$ catalysts, which only delivered a yield of ≈14.7%, ≈2.7%, ≈3.6%, and ≈5.2%, respectively. The turnover number (TON, $mol_{reactant}/mol_{Ru}$) of Ru_3O_2/rGO catalysts for this oxidative dehydrogenation reaction is determined to be 17.22 (Figure 3b), much higher than that of Ru/C (2.94), RuO_2 (0.54), $Ru_3(CO)_{12}$ (0.72), and $Ru(acac)_3$ (1.04) catalysts. In addition, the Ru_3O_2/rGO shows a negligible activity declination after ten catalytic cycles, suggesting its high durability and recyclability (Figure S19, Supporting Information). Ru_3O_2/rGO represents one of the top performers among typical heterogeneous catalysts for oxidative dehydrogenation of THQ under similar reaction conditions (Table S2, Supporting Information).
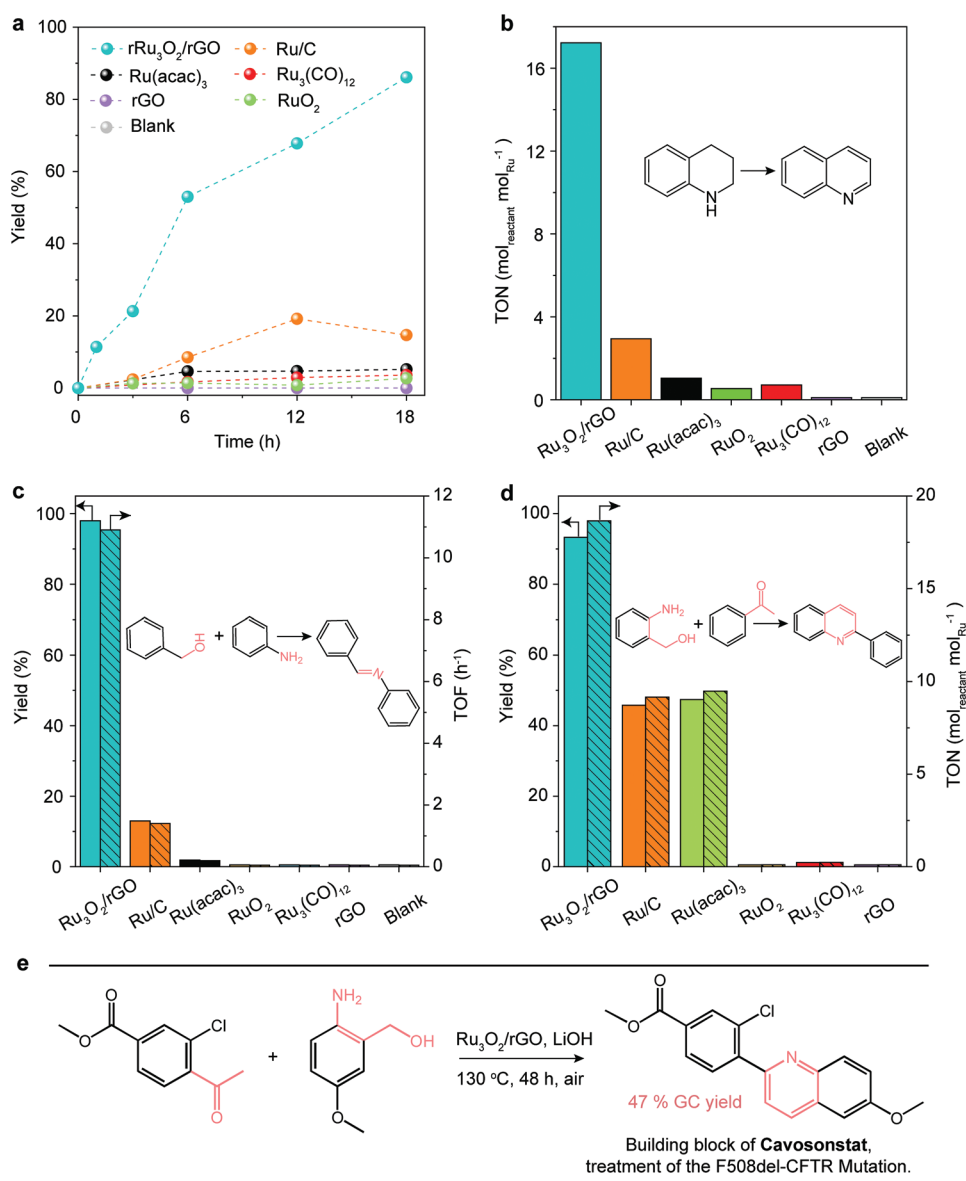
Figure 3. Catalytic performance of Ru$_3$O$_2$/rGO for various oxidative dehydrogenation reactions. a) Ru$_3$O$_2$/rGO and reference catalysts for the oxidative dehydrogenation of THQ to quinoline. b) A TON comparison of Ru$_3$O$_2$/rGO and reference catalysts. c) Yield and TOF comparison of Ru$_3$O$_2$/rGO and reference catalysts for the synthesis of imines from benzyl alcohol, aniline, and O$_2$. d) Yield and TON comparison of Ru$_3$O$_2$/rGO and reference catalysts for Friedländer synthesis. e) The synthesis of Cavosonstat derivative by Ru$_3$O$_2$/rGO catalysts. The related ^{1}H NMR and ^{13}C NMR data of raw materials and products were provided in Figures S22–S25 (Supporting Information).

We further evaluated the catalytic properties of Ru$_3$O$_2$/rGO for another more complex reaction to demonstrate the superiority of the Ru$_3$O$_2$ active sites for oxidative dehydrogenation reaction, namely, the synthesis of imines from benzyl alcohol, aniline, and O$_2$ gas. Typically. this reaction proceeds through these two key steps[31]: i) the oxidation of benzyl alcohol to form benzaldehyde, ii) benzaldehyde reacts with aniline to produce imines. Notably, the step (ii) can occur even without any catalysts in toluene at 90 °C (Figure S20, Supporting Information). Thus, step (i) is likely to be the rate-determining step for the overall reaction. Ru$_3$O$_2$/rGO delivers the imine yield of ≈99% and selectivity of ≈99% after 15 h (Figure 3c). In sharp contrast, Ru/C (10 wt.%) catalysts only offer a low yield (≈13%) of the

imines. TOF catalyzed by Ru$_3$O$_2$/rGO reaches up to 10.9 h^{-1}, ≈7.8 and 218 times larger than commercial Ru/C (10 wt.%; 1.4 h^{-1}) and RuO$_2$ (0.05 h^{-1}) catalyst, respectively (Figure 3c). Oxidative dehydrogenation is also a fundamental reaction in the formation of many heterocycles including Friedländer synthesis of quinolines from *ortho*-aminobenzyl alcohol and ketones that typically involves two oxidative dehydrogenation steps. In the first step, *ortho*-aminobenzyl alcohol is converted into reactive ortho-aminobenzaldehyde, and the meta-stable dihydroquinoline is transformed into quinoline in the second step. We also carried out additional catalyst screening on Friedländer synthesis (Figure 3d) to confirm that Ru$_3$O$_2$/rGO can tackle more complex oxidative dehydrogenation reactions. It is found that

ADVANCED
SCIENCE NEWS
www.advancedsciencenews.com

ADVANCED
FUNCTIONAL
MATERIALS
www.afm-journal.de

offers the best performance among many other homogeneous ($Ru(acac)_3$, $Ru_3(CO)_{12}$) and heterogeneous catalysts (10% Ru/C and RuO_2). Furthermore, we explored the synthesis of a Cavosonstat derivative (a F508del-CFTR mutation treatment medicine) by Friedländer synthesis under the optimized condition (Figure 3e). Ru_3O_2/rGO delivered a yield of 47% for the synthesis of Cavosonstat derivative in one step, in contrast to a yield of 46% in five-step reactions obtained by traditional Pd-catalyzed Suzuki coupling.[32] All these results demonstrate a superior activity of the Ru_3O_2/rGO for catalyzing complex reactions that involve multiple reactants. Moreover, Ru_3O_2/rGO also shows good stability in complex reactions as reflected in the negligible loss in activity and negligible change in the density of Ru_3O_2 clusters for the recycled Ru_3O_2/rGO sample after the synthesis of imines (Figure S21, Supporting Information).

2.3. Theoretical Studies of the Catalytic Origin

To gain a deep understanding of catalytic origins, we first calculated the electronic structures of Ru_3O_2/rGO SCC in comparison with those of Ru NPs and the hypothetical Ru_1/rGO SAC. Theoretical Ru_1/rGO model contains RuO active site anchored in monovacancy in graphene, while Ru NPs were modeled with representative Ru(0001) surface (refer to details in Computational Method Section in Supporting Information). Distinct from zero-valence of Ru atom in Ru NPs, Bader charge analysis reveals that Ru atom in rGO-Ru_1 SAC loses 0.6 e^-, while terminal and middle Ru atom in Ru_3O_2/rGO lose 0.9 e^- and 1.1 e^-, respectively. A higher charge state predicted for Ru_3O_2 is also consistent with the observation of Ru(III) valence state, as revealed in XANES data, which facilitates the oxidative dehydrogenation reaction including one of the key hydrogen abstraction steps (as discussed in the next reaction pathway calculation).

Next, we analyzed the adsorption properties of two reactants (O_2 and THQ) over these active sites. We first considered the adsorption behavior of individual O_2, which adopts an end-on configuration over Ru_3O_2/rGO, but exhibits a side-on configuration over rGO-Ru_1 and Ru(0001) (**Figure 4**a–c). The adsorption energies of O_2 are determined to be –0.6 eV for Ru_3O_2/rGO, –2.49 eV for rGO-Ru_1, and –1.99 eV for Ru(0001). Projected density of states (PDOS; Figure 4d–f) reveals that empty O_2 spin-down LUMO before adsorption (upper panels), gains electrons from interaction with catalytic center upon adsorption (lower panels), which thus gets partially filled. Electron transfer from Ru_3O_2/rGO to O_2 is determined to be 0.5 e^-, much lower than that over (0.7 e^-) rGO-Ru_1 and (0.9 e^-) Ru(0001). All these observations point out a strong electronic interaction and adsorption of O_2 over rGO-Ru_1 and Ru(0001), which tends to block active sites of rGO-Ru_1 for subsequent interaction with THQ. In contrast, weak electronic interaction of O_2 with Ru_3O_2/rGO is mainly contributed from the hybridization between Ru dz^2 orbital and O_2 pz orbital, leading to approximately half-filled Ru d orbitals near the E_f (Figure S26, Supporting Information). In addition, we also studied the adsorption of individual THQ molecule over these active sites. It is noted that THQ tends to form weak hydrogen bonds over Ru_3O_2 (Figure 4a), in contrast to strong N–Ru covalent bonds of THQ over both rGO-Ru_1 (Figure 4b) and Ru(0001) (Figure 4c).

The adsorption energy of THQ for Ru_3O_2/rGO, rGO-Ru_1, and Ru (0001) is calculated to be –0.41 eV, –1.24 eV, and –1.05 eV, respectively. The weak interaction of individual THQ and O_2 molecules over Ru_3O_2/rGO prompts the catalytic conversion of quinoline, as compared to rGO-Ru_1, and Ru (0001).

We also examined the co-adsorption of THQ with pre-adsorption of O_2 over these active sites (Figure S27, Supporting Information). It is noted that the co-adsorption of these two reactants is not allowed over rGO-Ru_1 catalyst due to limited space. For Ru_3O_2/rGO catalyst, O_2 molecule retains end-on configuration and bonds with one terminal Ru atom, whereas THQ interacts with two oxygen atoms in Ru_3O_2 site through hydrogen bonding. It is observed that pre-adsorption of O_2 slightly enhances the adsorption of THQ over Ru_3O_2/rGO, resulting in an increase of the adsorption energy from –0.41 eV to –0.45 eV. In contrast, strong adsorption of THQ on Ru(0001) is further enhanced from –1.05 to –1.20 eV by pre-adsorption of O_2. These results reveal that weaker adsorption properties of Ru_3O_2/rGO for two reactants (THQ and O_2) are more favorable for catalytic conversion than Ru NPs (strong adsorption) and rGO-Ru_1 (lack of ability for co-adsorption).

Apart from the adsorption of reactants, we also studied the desorption of the final product, quinoline. Our calculations show that the desorption energy of quinoline is 0.1, 1.78, and 1.28 eV for Ru_3O_2/rGO, rGO-Ru_1, and Ru(0001), respectively. Large desorption energy makes it harder to desorb products from the active site. All the calculation results reveal excellent adsorption of reactants, desorption of product, and synergistic properties of Ru_3O_2/rGO for the oxidative dehydrogenation of THQ, superior to Ru_1/rGO SACs and Ru NP catalysts.

We then calculated the thermal energy profiles of two plausible reaction pathways for oxidative dehydrogenation of THQ over the Ru_3O_2/rGO catalysts to further highlight the unique catalytic role of oxygen dopant in Ru_3O_2/rGO SCC. The pathway I (black line in Figure 4g) involves a few key steps: i) co-adsorption: the reaction starts with co-adsorption of O_2 and THQ with adsorption energy of –1.05 eV, as detailed in the above co-adsorption part. ii) First H abstraction: two O atoms (one from the unbonded O atom of adsorbed O_2 molecule, another one from the adjacent O dopant atom of Ru_3O_2) totally abstract two H atoms simultaneously from the amino group and neighboring CH_2 (C1) group, respectively. This dehydrogenation step is slightly endothermal with an energy of 0.03 eV required. Due to the presence of O dopant in Ru_3O_2, the H abstraction process proceeds very differently from the reported reaction mechanism, wherein the H atom is usually abstracted one by one.[33–36] iii) Second H abstraction: the remaining H atom on the C1 group is transferred to HO-O* on terminal Ru atom to form the first H_2O molecule with an energy decrease of 0.05 eV. iv) First equilibration: as the H_2O molecule is still adsorbed on the terminal Ru atom, the intramolecular H atom transfers from the second neighboring CH_2 group (C2) to C1 with an energy decrease of 1.09 eV to reach the first equilibration of reaction, generating the 1,4-dihydroquinoline (1,4-DHQ) intermediates. v and vi): First H_2O release and H transfer: the H_2O molecule desorbs from the terminal Ru atom with desorption energy of 0.2 eV, and then the H atom on the middle Ru atom transfers to the O atom residing at the terminal Ru atom to form OH*. This intramolecular H transfer costs energy of 0.67 eV. vii) Third H abstraction: the remaining H atom
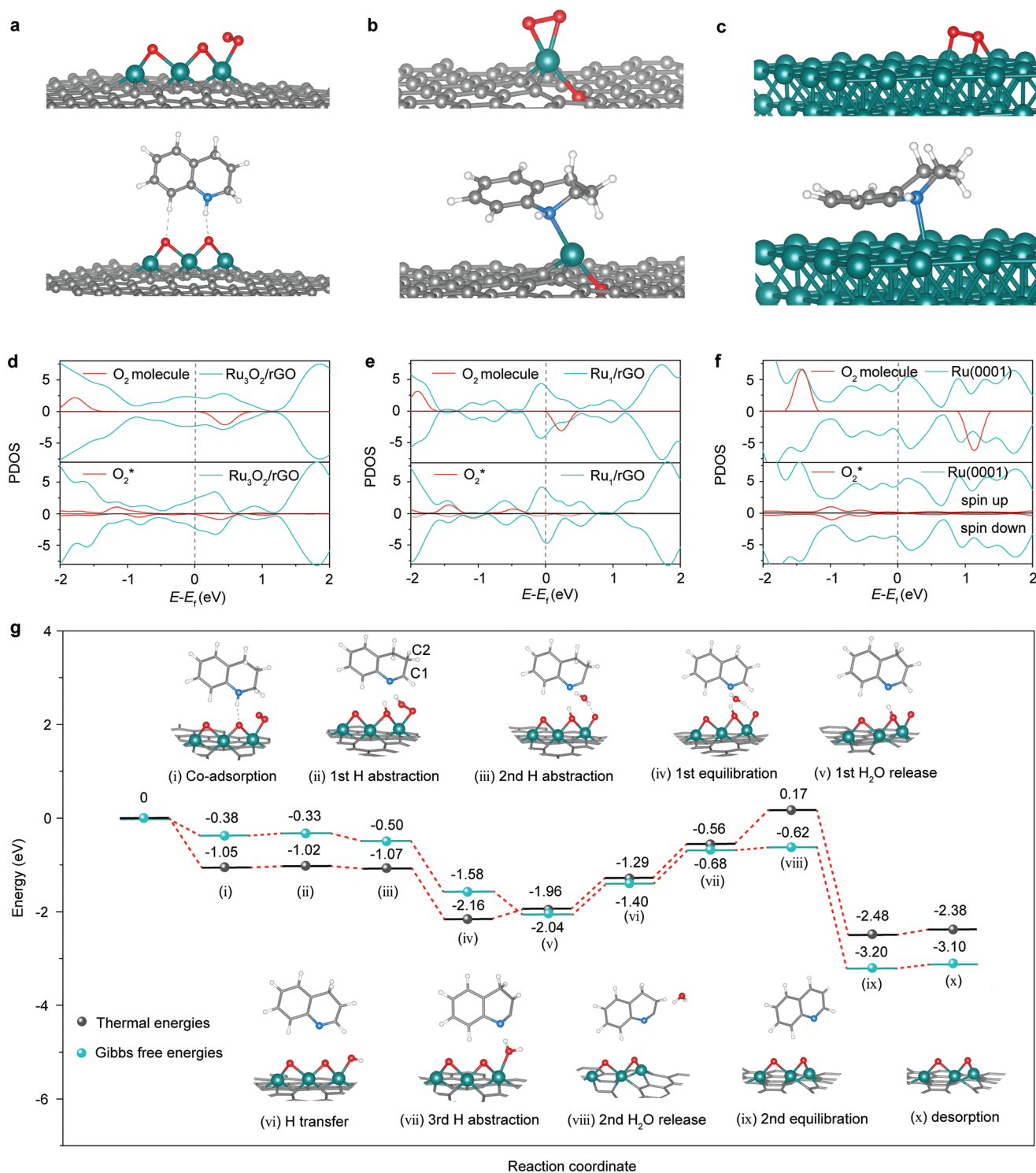
Figure 4. Theoretical calculations for probing the catalytic origin of Ru₃O₂/rGO for oxidative dehydrogenation of THQ. a–c) Theoretical models of Ru₃O₂/rGO, rGO-Ru₁, and Ru NPs with adsorbed O₂ (upper panel) and THQ (lower panel), respectively. d–f) PDOS analysis of Ru₃O₂/rGO, rGO-Ru₁, and Ru NPs before (upper panel) and after O₂ adsorption (lower panel). g) Reaction pathway and computational energy profile of the oxidative dehydrogenation of THQ to quinoline over Ru₃O₂/rGO catalysts. The blue and black lines represent Gibbs free energies and thermal energies, respectively.

from the C1 site moves to OH* at the terminal Ru site, and then a second H_2O molecule is generated with an energy increase of 0.73 eV. This H abstraction step is endothermal with much

more energy required than previous steps, however, it is much lower than that on Ru(0001), which shows an energy increase of 1.43 eV (Figure S28, Supporting Information). The superior

H abstraction ability of Ru_3O_2 than that of Ru NPs is due to the higher oxidation state of Ru in Ru_3O_2. viii) Second H_2O release: the second H_2O molecule is desorbed from the terminal Ru atom with an energy of 0.73 eV input, which is the same as the third H abstraction process. ix and x) Second equilibration and desorption: intramolecular H atom transfers from the C3 site to the C1 site, then quinoline is produced with an energy drop of 2.65 eV and followed by desorption from the Ru_3O_2/rGO with a small amount of energy needed (0.10 eV). Our calculations reveal that the production and desorption of the second H_2O molecule need to overcome reaction energy of 0.73 eV, which can be readily surmounted upon heating. The calculated Gibbs free energies (blue lines) along the reaction path are plotted together with thermal energies (black lines) in Figure 4. The free energy calculations are different from thermal energies mainly in the first four and last three elementary steps, while both free energy and thermal energy profile predict that the transfer of the third H (from step vi to vii) provides the largest energy difference of 0.73 and 0.72 eV from thermal energies and free energies, respectively. Selective oxidation is also considered from a theoretical perspective (Figures S29 and S30, Supporting Information), suggesting it is more likely to generate 1,4-DHQ intermediates due to a lower energy cost (0.73 eV) than that of 1,2-DHQ intermediates (0.87 eV). We also considered pathway ii (Figure S31, Supporting Information), which differs from pathway I in step (vi). In step (vi) in pathway II, THQ intermediate undergoes a third H abstraction process, followed by the second equilibrium process (step vii), which shows a higher energy cost (1.38 eV).

3. Conclusion

In summary, we demonstrated an interface confinement strategy for the synthesis of atomically precise high-density single Ru_3O_2 nanoclusters on rGO. Two oxygen atoms in the Ru_3O_2 motif efficiently weaken the interaction strength between THQ and Ru_3O_2 via forming hydrogen bonds, and dramatically deplete the density of states near the Fermi level that increases the oxidative activity of Ru cluster for hydrogen abstraction. As a result, Ru_3O_2/rGO SCC shows superior catalytic performance than Ru NPs, RuO_2 NPs, and homogeneous single/multiple-site Ru catalysts for the oxidative dehydrogenation of THQ and other complex oxidative reactions. Our findings provide an efficient strategy to design high-density single metal cluster catalysts, whose activity and catalytic scopes can be further enhanced via heteroatom doping to tackle more complex chemical transformations.

Supporting Information

Supporting Information is available from the Wiley Online Library or from the author.

Conflict of Interest

The authors declare no conflict of interest.

Data Availability Statement

The data that support the findings of this study are available from the corresponding author upon reasonable request.

[1] B. Qiao, A. Wang, X. Yang, L. F. Allard, Z. Jiang, Y. Cui, J. Liu, J. Li, T. Zhang, *Nat. Chem.* **2011**, *3*, 634.
[2] J.-C. Liu, X.-L. Ma, Y. Li, Y.-G. Wang, H. Xiao, J. Li, *Nat. Commun.* **2018**, *9*, 1610.
[3] E. C. Tyo, S. Vajda, *Nat. Nanotechnol.* **2015**, *10*, 577.
[4] X.-L. Ma, J.-C. Liu, H. Xiao, J. Li, *J. Am. Chem. Soc.* **2018**, *140*, 46.
[5] H. Rong, S. Ji, J. Zhang, D. Wang, Y. Li, *Nat. Commun.* **2020**, *11*, 5884.
[6] Y. Pan, Y. Zhang, Z. Liu, C. Chen, Y. Li, *Matter* **2020**, *2*, 78.
[7] L. Liu, A. Corma, *Chem. Rev.* **2018**, *118*, 4981.
[8] C. Yao, N. Guo, S. Xi, C.-Q. Xu, W. Liu, X. Zhao, J. Li, H. Fang, J. Su, Z. Chen, H. Yan, Z. Qiu, P. Lyu, C. Chen, H. Xu, X. Peng, X. Li, B. Liu, C. Su, S. J. Pennycook, C.-J. Sun, J. Li, C. Zhang, Y. Du, J. Lu, *Nat. Commun.* **2020**, *11*, 4389.
[9] A. Wang, J. Li, T. Zhang, *Nat. Rev. Mater.* **2018**, *2*, 65.
[10] X.-F. Yang, A. Wang, B. Qiao, J. Li, J. Liu, T. Zhang, *Acc. Chem. Res.* **2013**, *46*, 1740.
[11] Y. Chen, S. Ji, C. Chen, Q. Peng, D. Wang, Y. Li, *Joule* **2018**, *2*, 1242.
[12] J. Gu, M. Jian, L. Huang, Z. Sun, A. Li, Y. Pan, J. Yang, W. Wen, W. Zhou, Y. Lin, H.-J. Wang, X. Liu, L. Wang, X. Shi, X. Huang, L. Cao, S. Chen, X. Zheng, H. Pan, J. Zhu, S. Wei, W.-X. Li, J. Lu, *Nat. Nanotechnol.* **2021**.
[13] E. Guan, J. Ciston, S. R. Bare, R. C. Runnebaum, A. Katz, A. Kulkarni, C. X. Kronawitter, B. C. Gates, *ACS Catal.* **2020**, *10*, 9065.
[14] T. Ding, X. Liu, Z. Tao, T. Liu, T. Chen, W. Zhang, X. Shen, D. Liu, S. Wang, B. Pang, D. Wu, L. Cao, L. Wang, T. Liu, Y. Li, H. Sheng, M. Zhu, T. Yao, *J. Am. Chem. Soc.* **2021**, *143*, 11317.
[15] S. Tian, B. Wang, W. Gong, Z. He, Q. Xu, W. Chen, Q. Zhang, Y. Zhu, J. Yang, Q. Fu, C. Chen, Y. Bu, L. Gu, X. Sun, H. Zhao, D. Wang, Y. Li, *Nat. Commun.* **2021**, *12*, 3181.
[16] W. Ye, S. Chen, Y. Lin, L. Yang, S. Chen, X. Zheng, Z. Qi, C. Wang, R. Long, M. Chen, J. Zhu, P. Gao, L. Song, J. Jiang, Y. Xiong, *Chem* **2019**, *5*, 2865.

**ADVANCED
SCIENCE NEWS**

www.advancedsciencenews.com

**ADVANCED
FUNCTIONAL
MATERIALS**

www.afm-journal.de

[17] S. Ji, Y. Chen, Q. Fu, Y. Chen, J. Dong, W. Chen, Z. Li, Y. Wang, L. Gu, W. He, C. Chen, Q. Peng, Y. Huang, X. Duan, D. Wang, C. Draxl, Y. Li, *J. Am. Chem. Soc.* **2017**, *139*, 9795.

[18] S. Tian, Q. Fu, W. Chen, Q. Feng, Z. Chen, J. Zhang, W.-C. Cheong, R. Yu, L. Gu, J. Dong, J. Luo, C. Chen, Q. Peng, C. Draxl, D. Wang, Y. Li, *Nat. Commun.* **2018**, *9*, 2353.

[19] S. Ji, Y. Chen, S. Zhao, W. Chen, L. Shi, Y. Wang, J. Dong, Z. Li, F. Li, C. Chen, Q. Peng, J. Li, D. Wang, Y. Li, *Angew. Chem., Int. Ed.* **2019**, *58*, 4271.

[20] J. Jiao, R. Lin, S. Liu, W.-C. Cheong, C. Zhang, Z. Chen, Y. Pan, J. Tang, K. Wu, S.-F. Hung, H. M. Chen, L. Zheng, Q. Lu, X. Yang, B. Xu, H. Xiao, J. Li, D. Wang, Q. Peng, C. Chen, Y. Li, *Nat. Chem.* **2019**, *11*, 222.

[21] L. Zhang, R. Si, H. Liu, N. Chen, Q. Wang, K. Adair, Z. Wang, J. Chen, Z. Song, J. Li, M. N. Banis, R. Li, T.-K. Sham, M. Gu, L.-M. Liu, G. A. Botton, X. Sun, *Nat. Commun.* **2019**, *10*, 4936.

[22] G. S. Attard, J. C. Glyde, C. G. Göltner, *Nature* **1995**, *378*, 366.

[23] S. Yang, X. Feng, L. Wang, K. Tang, J. Maier, K. Müllen, *Angew. Chem., Int. Ed.* **2010**, *49*, 4795.

[24] H. Yan, Y. Lin, H. Wu, W. Zhang, Z. Sun, H. Cheng, W. Liu, C. Wang, J. Li, X. Huang, T. Yao, J. Yang, S. Wei, J. Lu, *Nat. Commun.* **2017**, *8*, 1070.

[25] L. Zhang, J. M. T. A. Fischer, Y. Jia, X. Yan, W. Xu, X. Wang, J. Chen, D. Yang, H. Liu, L. Zhuang, M. Hankel, D. J. Searles, K. Huang, S. Feng, C. L. Brown, X. Yao, *J. Am. Chem. Soc.* **2018**, *140*, 10757.

[26] X. Zhu, D. Zhang, C.-J. Chen, Q. Zhang, R.-S. Liu, Z. Xia, L. Dai, R. Amal, X. Lu, *Nano Energy* **2020**, *71*, 104597.

[27] Z. Lu, B. Wang, Y. Hu, W. Liu, Y. Zhao, R. Yang, Z. Li, J. Luo, B. Chi, Z. Jiang, M. Li, S. Mu, S. Liao, J. Zhang, X. Sun, *Angew. Chem., Int. Ed.* **2019**, *58*, 2622.

[28] X. Li, Y. Fang, J. Wang, H. Fang, S. Xi, X. Zhao, D. Xu, H. Xu, W. Yu, X. Hai, C. Chen, C. Yao, H. B. Tao, A. G. R. Howe, S. J. Pennycook, B. Liu, J. Lu, C. Su, *Nat. Commun.* **2021**, *12*, 2351.

[29] X. Li, Y. Fang, J. Wang, B. Wei, K. Qi, H. Y. Hoh, Q. Hao, T. Sun, Z. Wang, Z. Yin, Y. Zhang, J. Lu, Q. Bao, C. Su, *Small* **2019**, *15*, 1902427.

[30] Z. Chen, J. Song, X. Peng, S. Xi, J. Liu, W. Zhou, R. Li, R. Ge, C. Liu, H. Xu, X. Zhao, H. Li, X. Zhou, L. Wang, X. Li, L. Zhong, A. I. Rykov, J. Wang, M. J. Koh, K. P. Loh, *Adv. Mater.* **2021**, *33*, 2101382.

[31] J. Qin, Y. Long, W. Wu, W. Zhang, Z. Gao, J. Ma, *J. Catal.* **2019**, *371*, 161.

[32] Z. Chen, J. Liu, M. J. Koh, K. P. Loh, *Adv. Mater.* **2021**, 2103882.

[33] M. K. Sahoo, G. Jaiswal, J. Rana, E. Balaraman, *Chem. Eur. J.* **2017**, *23*, 14167.

[34] M. F. Zheng, J. L. Shi, T. Yuan, X. C. Wang, *Angew. Chem., Int. Ed.* **2018**, *57*, 5487.

[35] D. Xu, H. Zhao, Z. Dong, J. Ma, *ChemCatChem* **2019**, *11*, 5475.

[36] Z. Zhang, W. Liu, Y. Zhang, J. Bai, J. Liu, *ACS Catal.* **2021**, *11*, 313.

2200933 (9 of 9)